Two-atom Rydberg blockade using direct 6*S* to *nP* excitation

A. M. Hankin,[1,2] Y.-Y. Jau,[1] L. P. Parazzoli,[1] C. W. Chou,[1] D. J. Armstrong,[1] A. J. Landahl,[1,2] and G. W. Biedermann[1,2,*]

[1]*Sandia National Laboratories, Albuquerque, New Mexico 87185, USA*

[2]*Center for Quantum Information and Control (CQuIC), Department of Physics and Astronomy, University of New Mexico, Albuquerque, New Mexico 87131, USA*

(Received 13 January 2014; published 13 March 2014)

We explore a single-photon approach to Rydberg state excitation and Rydberg blockade. Using detailed theoretical models, we show the feasibility of direct excitation, predict the effect of background electric fields, and calculate the required interatomic distance to observe Rydberg blockade. We then measure and control the electric field environment to enable coherent control of Rydberg states. With this coherent control, we demonstrate Rydberg blockade of two atoms separated by 6.6(3) μm. When compared with the more common two-photon excitation method, this single-photon approach is advantageous because it eliminates channels for decoherence through photon scattering and ac Stark shifts from the intermediate state while moderately increasing Doppler sensitivity.

DOI: 10.1103/PhysRevA.89.033416 PACS number(s): 32.80.Ee, 32.80.Qk, 32.10.Dk, 32.70.Cs

I. INTRODUCTION

The large polarizability of high principal quantum number n Rydberg states gives rise to exotic many-body interactions as well as an extreme sensitivity to the electric field environment. Precision spectroscopy of such states allows for a variety of exciting demonstrations in metrology, fundamental quantum mechanics, and quantum information. For example, cold Rydberg atoms employed as near-surface electric field sensors enable characterization of both field amplitude and source. This includes experiments that explore near-surface field spectral density [1], induced dipole moments for surface adatoms [2], and insulator charging on an atom chip [3]. Large Rydberg state polarizabilities also enable long-range electric dipole-dipole interactions (EDDIs) between Rydberg atoms, yielding strongly correlated systems through the Rydberg blockade effect. Recent experiments use Rydberg blockade to observe entanglement between neutral atoms [4,5], a controlled-NOT quantum gate [6], and collective many-body Rabi oscillations [7]. These advances parallel an ever-evolving approach to Rydberg state control. In this paper, we demonstrate Rydberg blockade using a unique single-photon excitation approach to precision Rydberg spectroscopy.

The ionization threshold for ground-state alkali-metal atoms ranges from 3.9 to 5.4 eV, setting the energy scale for excitation to high-lying Rydberg states. In practice, this is commonly accomplished with two-photon excitation, where the ground and Rydberg states couple together through an intermediate state [8]. Two-photon excitation avoids deep, ultraviolet (UV) wavelengths making the implementation technologically simpler. However, photon scattering and ac Stark shifts from the intermediate state introduce avenues for decoherence, frequency noise, and dipole forces complicating two-photon experiments [9]. Minimizing photon scattering is of particular importance when using Rydberg-dressed atoms to create tunable, long-lived, many-body interactions in a quantum gas [10]. For example, the adiabatic quantum optimization protocol described in [11] is predicted to achieve a substantially higher fidelity in the absence of photon scattering from the intermediate state. At present, studies of Rydberg blockade with a single-photon transition are rare. Previous work utilized single-photon excitation with pulsed UV lasers to perform high-resolution spectroscopy of Rydberg states [12] and to detect Rydberg blockade as a bulk effect [13]. Still, direct excitation using a continuous-wave (cw) UV laser, which would allow for coherent control of single atoms, has not been demonstrated.

Here, we show coherent control of blockaded $84P_{3/2}$ states of two single ^{133}Cs atoms using a cw UV laser at 319 nm. Construction of this UV laser is informed by calculations for the required wavelength and intensity. With over 300 mW of 319-nm light at the output of the laser, we demonstrate a Rabi frequency of over 2 MHz with this approach, in agreement with our predictions for resonance frequency and oscillator strength. Given this success, we further develop our model to determine a regime for observing Rydberg blockade between two atoms, and we observe and analyze Rydberg blockade for the $84P_{3/2}$ state.

This paper is organized in the following way: In Sec. II, we establish a detailed model for single-photon excitation to Rydberg P states that includes predictions for the Rydberg spectrum and oscillator strengths. We next use this model to design a cw UV laser system, the details of which are found in Sec. III. In Sec. IV, we describe the experimental technique used to trap and control two atoms in close proximity. In Sec. V, we use our single-atom control in combination with the UV laser system to measure the background electric field inherent to our apparatus. We then implement active control and suppression of the electric field to enable coherent control of the atom. In Sec. VI, we present our study of the Rydberg blockade, including a model of the Rydberg spectrum for two atoms as a function of interatomic spacing and an experimental demonstration of the blockade effect in this system. We conclude with applications where the single-photon excitation approach is expected to excel.

II. SINGLE-PHOTON EXCITATION MODEL

We use a theoretical model for single-photon excitation of high-n states to accurately calculate the Rydberg spectrum

*gbieder@sandia.gov

and $6S_{1/2} \rightarrow nP$ transition oscillator strengths. The spectra of alkali-metal atoms are predicted with high precision by quantum defect theory (QDT) [14]. Using QDT, the energies of bound electronic states E are given by

$$E(n,\ell,j) = E_\infty - \frac{R_{\mathrm{Cs}}}{[n-\delta(n,\ell,j)]^2}, \tag{1}$$

where ℓ is the orbital angular quantum number, j is the total angular momentum quantum number, E_∞ is the ionization threshold energy, R_{Cs} is the Rydberg constant for cesium, and δ is the quantum defect. A method for calculating $\delta(n,\ell,j)$ is found in [15] where the observed Rydberg spectra are fit to a power series in n. The spectrum of ^{133}Cs calculated with Eq. (1) is found in Fig. 1. The optical frequency for excitation directly from $6S_{1/2}$ to $84P_{3/2}$ is calculated to be 941 030 GHz.

Given the transition frequency, we require the transition oscillator strength f to determine if single-photon excitation is feasible with current technology. A semiempirical method for calculating f is found in [16]. Computing f requires knowledge of the radial wave functions and the associated radial matrix elements $\langle n'\ell' j'|r|n\ell j\rangle$. The radial wave function is calculated by substituting the energies predicted by QDT into Schrödinger's equation and $\langle n'\ell' j|r|n\ell j\rangle$ is then computed through numerical integration. We find the oscillator strengths for the $6S_{1/2}$ to $84P$ transitions are $f(6S_{1/2} \rightarrow 84P_{3/2}) = 6\times10^{-8}$ and $f(6S_{1/2} \rightarrow 84P_{1/2}) = 2\times10^{-12}$. The 10^4 order of magnitude difference between the calculated oscillator strengths is a property that is unique to cesium when compared with the other alkali-metal atoms. The divergence of the principal-series doublet $(6S_{1/2} \rightarrow nP_{3/2,1/2})$ oscillator strength ratio for large n is a well-known phenomenon that arises with the inclusion of spin-orbit effects and the core polarizability [16–19]. This result favors exciting to $nP_{3/2}$ states in the interest of reducing laser power requirements.

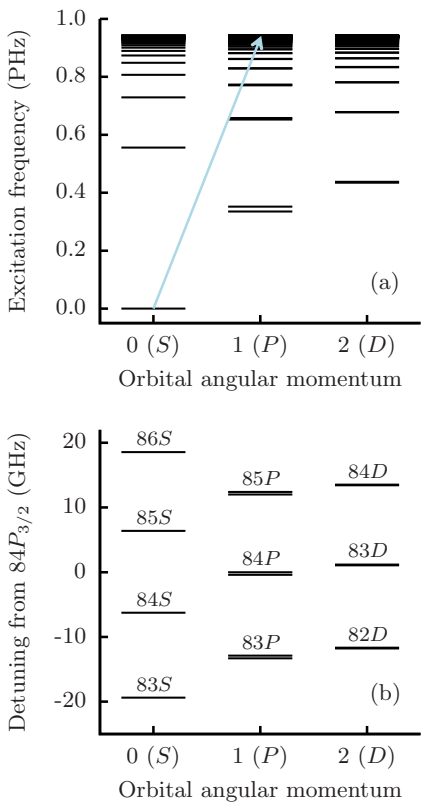

FIG. 1. (Color online) Spectrum of cesium using QDT. (a) Spectrum from the ground state through $n = 100$. The experimental work in this paper focuses on the $6S_{1/2} \rightarrow 84P_{3/2}$ transition, labeled by the blue arrow. (b) Detailed spectrum near $84P_{3/2}$. Fine-structure splitting in the nP_j and nD_j states is included. nP states appear broader due to splitting between $nP_{1/2}$ and $nP_{3/2}$. Fine structure between the nD states is ~100 MHz and therefore not well resolved on this scale.

While the oscillator strength determines the scaling of Rabi frequency Ω with laser intensity, it does not directly set a lower limit on laser power. Instead, we must consider limits on the Rydberg laser waist and the coherence time between the Rydberg state $|r\rangle$ and the ground state $|g\rangle$ set by experimental conditions. For a reasonable atom temperature of 10 μK and a trap waist of 1 μm, the atom velocity spread limits the linewidth to order 100 kHz and the spatial spread to order 1 μm. We target a Rabi frequency on the order of $\Omega/2\pi =$ 1 MHz and a laser waist of 10 μm to avoid decoherence and intensity fluctuations due to atom motion. Combining the limitation on Ω with the targeted waist, we find that 16 mW of 319-nm light is sufficient to observe state evolution that is dominated by coherent dynamics. The design for the cw UV laser described in the following section surpasses this requirement.

III. RYDBERG LASER

The cw UV laser is constructed using sum frequency generation (SFG) followed by frequency doubling. A similar approach tailored for 313 nm is found in [20]. We first produce 638-nm light using SFG and then generate the 319-nm light via frequency doubling. The SFG begins with 1574- and 1071-nm fiber laser sources with 18- and 60-mW output powers, respectively. Both lasers seed commercial 5-W fiber amplifiers and the resulting light is combined and passed through a periodically poled lithium niobate (PPLN) crystal generating 1.1 W of 638-nm light. The output of the PPLN crystal is frequency doubled from 638 to 319 nm with a BBO (β-BaB_2O_2) crystal and results in greater than 300 mW at this wavelength. From the spectrum shown in Fig. 1, we predict the laser's frequency can be tuned to reach $84P$ through $120P$. Upon exiting the doubling cavity, the beam is shaped into a Gaussian profile, passed through two AOMs for intensity stabilization and switching, and focused down on the two atoms with a measured $1/e^2$ radius of 12.9(3) μm. This results in the two atoms experiencing a maximum intensity of 60 kW/cm^2 after accounting for the losses incurred at each optic.

The frequency of the Rydberg laser is stabilized to an ultralow expansion, high-finesse (HF) cavity [21] at 638 nm via a multistage servo architecture (Fig. 2). A direct lock to the cavity-frequency reference is precluded by characteristics of the fiber laser sources. Frequency noise on the 638-nm light exceeds the 75-kHz cavity linewidth as well as the bandwidth of the frequency control of the fiber lasers. We overcome this by dividing low- and high-bandwidth frequency stabilization into two paths.

Low-bandwidth frequency control is implemented by first stabilizing the 638-nm light to a low-finesse (LF) cavity with a

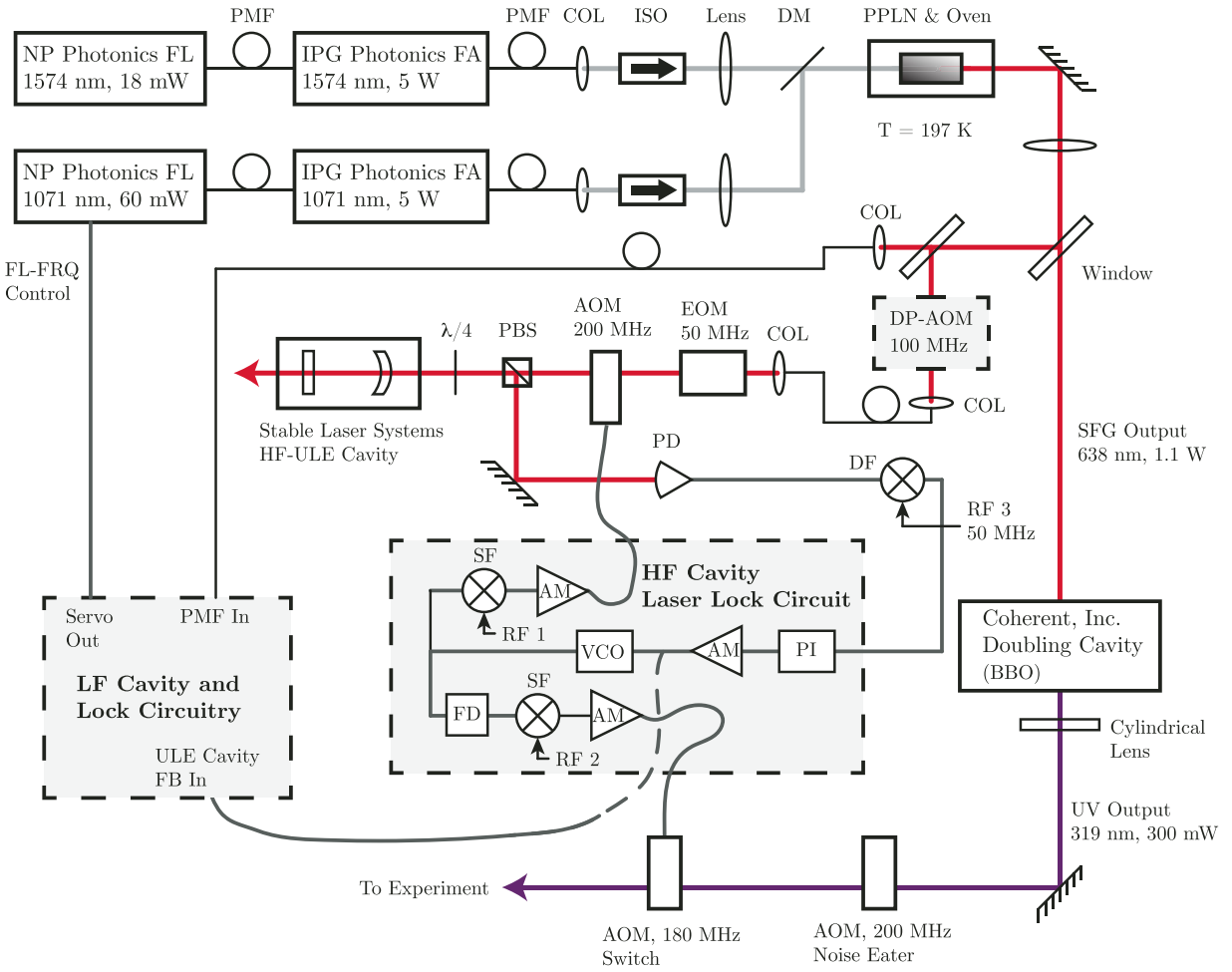

FIG. 2. (Color online) Diagram of UV laser system. Frequency summing in a PPLN crystal of two fiber laser systems yields 638-nm light and frequency doubling of this light in BBO generates UV light at 319 nm. Laser frequency is stabilized using a multistaged servo with an ultralow expansion (ULE), high-finesse (HF) cavity as the primary reference. $\lambda/4$: quarter-wave plate; AM: voltage amplifier; COL: fiber collimation package; DF: difference frequency; DM: dichroic mirror; DP-AOM: double-pass acousto-optic modulator system; EOM: electro-optic modulator; FA: fiber amplifier; FB: feedback; FD: frequency doubling; FL: fiber laser; FL-FRQ: voltage control of fiber laser frequency; ISO: optical isolator; LF: low finesse; PD: photodiode; PI: proportional-integral feedback; PMF: polarization maintaining fiber; SF: sum frequency; rf: radio frequency source; VCO: voltage controlled oscillator.

5-MHz linewidth. This frequency stabilization stage narrows the laser linewidth through feedback to the 1071-nm fiber laser. Next, we split a small fraction of the 638-nm light along an optical path used to monitor and stabilize the light's frequency to the HF cavity. Because the LF cavity lock has narrowed the 638-nm linewidth, we are able to directly lock the light along this path to the HF cavity. The HF cavity lock system consists of an electro-optic modulator (EOM), an AOM, and the HF cavity. The locking error signal is generated using the Pound-Drever-Hall technique where the EOM modulates the phase of the light while the response is monitored in reflected cavity signal. We then feedback to the drive frequency of the AOM to stabilize the frequency of the light to the cavity. However, because this AOM is not placed in the primary, high-power 638-nm beam path, the laser frequency at the atom does not directly benefit from the servo. This leaves the primary laser beam path susceptible to drifts in the LF cavity length with changes in temperature, pressure, and humidity. We avoid this issue using a low-bandwidth feedback loop that adjusts the LF cavity length to stabilize the frequency of the 638-nm light to the HF cavity resonance. The result of this portion of the locking system is a 638-nm linewidth of no more than 200 kHz along the high-power beam path.

The linewidth of the 319-nm light is narrowed further using high-bandwidth feed-forward control. While it is possible to use a closed-loop servo to directly stabilize the laser frequency by placing the control AOM directly in the high-power 638-nm beam path, we choose a feed-forward approach in favor of maximizing the UV power. The feed-forward control is accomplished by splitting the radio frequency (rf) signal used to stabilize the 638-nm laser to the HF cavity along a second path. This new path applies high-bandwidth corrections to the 319-nm laser frequency by modulating the drive frequency of an AOM in the UV beam path. The circuit compensates for the frequency doubling that occurs in the optical domain at the BBO crystal by placing a frequency doubler in the second rf path. This feed-forward architecture transfers the high-frequency content of the HF cavity lock to the UV light.

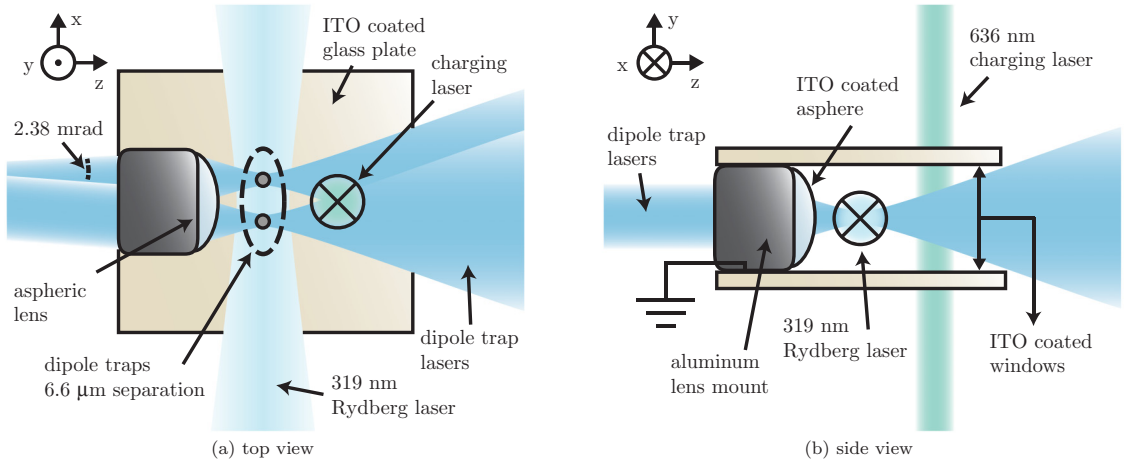

FIG. 3. (Color online) Diagram of the atom-trapping region. Two collimated 938-nm dipole trap beams with a 2.38-mrad relative angle pass through an aspheric lens resulting in two traps separated by 6.6(3) μm at the focal plane. A 319-nm laser, used to excite to Rydberg states, is focused down to a 12.9(4)-μm waist at the location of the atoms. The aspheric lens has a 112-nm ITO coating on the side facing the dipole traps and an antireflection (AR) coating for 852 nm on the opposite side. An aluminum cylinder is fixed concentric to the AR-coated side to shield against charging of this dielectric. The resulting assembly is fixed between two ITO-coated glass plates with a vacuum compatible, conductive epoxy. Each plate has an ITO coating on the side closest to the traps. The entire assembly is grounded. The top ITO plate is not shown in (a) for clarity. A 636-nm charging laser beam generates controlled charging on the ITO plates, which grants leverage over the background electric field environment. Figures are not to scale.

IV. EXPERIMENTAL APPARATUS

We create two optical dipole traps for quantum control of single cesium atoms in an all-glass, ultrahigh vacuum cell. The traps are generated inside a partial Faraday cage to control stray electric fields that perturb the Rydberg states. Rydberg excitation of these atoms is detected via atom loss as Rydberg states are ejected from the trap. By carefully tuning the optical parameters to minimize heating, we are able to reuse the same atoms for multiple experiments. The experimental system used to trap and probe two single ^{133}Cs atoms was built by modifying the setup described in [22]. The atoms are confined with a well-defined separation, in two far-off-resonant dipole traps using 938-nm light. The trapping light passes first through an acousto-optical modulator (AOM) and then through an in-vacuum aspheric lens with a 2.76-mm focal length. By driving the AOM at two frequencies (74.6 and 85.4 MHz), we generate two 8-mW beams whose propagation directions deviate by 2.38 mrad. This AOM-lens system results in two dipole traps separated by 6.6(3) μm [23] Both traps have a 1.26(1)-μm waist and a 21.1(1)-MHz trap depth for the atomic ground state. Once trapped, the atoms have a vacuum limited trap lifetime of approximately 7 s. We source the 938-nm light from a distributed feedback laser diode and find it necessary to filter elements of 852 and 895 nm from this laser (D_2 and D_1 transitions in ^{133}Cs) to avoid excessive heating that inhibits stable trapping.

The atoms are trapped 2.16 mm from the lens surface where background electric fields can be problematic for coherent control of Rydberg atoms [24]. We suppress these fields by coating the surface of the lens closest to the atom with a 112-nm layer of indium tin oxide (ITO). This transparent yet conductive coating is grounded to dissipate charging. To further protect against the influence of external electric fields, we surround the trapping region with a partial Faraday cage in vacuum by mounting the lens between two parallel glass plates that are also coated with ITO (Fig. 3). Using finite element analysis to approximate the solution to Laplace's equation for the electric potential, we calculate that this geometry suppresses electric fields external to the system by a factor of 1000.

The atoms are loaded into the dipole traps from a magneto-optical trap (MOT). The dissipative scattering force generated by the MOT cools atoms into the conservative pseudopotential of these traps. Once captured, the atoms continue to fluoresce on the D_2 transition of ^{133}Cs ($6S_{1/2} \rightarrow 6P_{3/2}$), and we spatially discriminate this signal to detect a loading event. This light is collected by the same aspheric lens used to produce the dipole traps and a dichroic mirror separates the 938-nm trapping light from this 852-nm fluorescence of the D_2 transition. After reflecting off the dichroic, the two beams of fluorescence are imaged at a plane coincident with a gold knife edge. The knife edge is positioned such that the image from one atom is reflected off of the gold surface, while the image from the other passes. Next, the fluorescence of each atom is coupled into separate 9-μm core fibers [25] that feed separate avalanche photodiodes (APDs). We find that this core size yields a near-optimal signal-to-noise ratio for single-atom detection in our apparatus. The technique we use to split the fluorescence beams is similar to the one developed by [5]. We adjust the MOT cloud density to operate both traps in the collisional blockade regime such that loading is limited to a maximum of one atom [26]. By waiting for a coincidence of bright fluorescence signals from both APDs, we load single atoms simultaneously in both traps. Once loaded, we switch off the loading process by extinguishing the MOT lasers and the quadrupole magnetic field. After a 10-ms wait period that allows for the magnetic field environment to stabilize and the MOT cloud to dissipate, we prepare the same atoms for the single-photon excitation experiment.

Before excitation, we further cool the atoms and prepare them in $|6S_{1/2}, F = 4, m_F = 0\rangle$. The atoms are cooled to 16.1(1) μK using polarization-gradient cooling [27]. The experimental details for this cooling process are found in [22]. For state preparation into $|F = 4, m_F = 0\rangle$, a quantization axis is defined with a 4.8-G magnetic field and the atoms are illuminated with π-polarized light resonant with $F = 4 \rightarrow F' = 4$ on the D_1 transition ($6S_{1/2} \rightarrow 6P_{1/2}$). We find the large bias magnetic field necessary to obtain an optical pumping efficiency of 95(2)% into the target state [28].

The cold $|F = 4, m_F = 0\rangle$ atoms are the starting point for the direct excitation experiments. These experiments begin 1 ms following state preparation using the 319-nm laser described in Sec. III. Just before excitation, the atoms are released into free flight to avoid perturbations in the ground-state energy from the dipole trap. They are then recaptured 1 μs after the excitation pulse extinguishes. The results of these experiments are found in Secs. V and VI. We detect population in the Rydberg state by taking advantage of the different trapping forces experienced by the ground and Rydberg states for an atom in a red-detuned optical dipole trap; while the ground state of the atom is trapped, a Rydberg state will experience an antitrapping potential [8] causing it to quickly eject from the dipole trap and allowing atom loss to signal Rydberg excitation [4].

We check for atom loss 1 ms after excitation, allowing ample time for a Rydberg state to leave the trapping region. For this check, we probe for atom fluorescence on the D_2 cycling transition ($F = 4 \rightarrow F' = 5$) for 500 μs with two counterpropagating detection lasers that are directed along the y axis (Fig. 3) superimposed with repump light on the $F = 3 \rightarrow F' = 4$ transition. A detection beam detuning of 5.0 MHz and an intensity of 17 mW/cm^2 optimally trades heating rate and signal-to-noise ratio. The APD that monitors fluorescence during detection measures an average number of photon counts of 8.4 and 0.51 for the bright (atom present) and dark (no atom) states, respectively. With a discriminator equating the bright-state with a measurement of greater than two counts, we achieve single-shot atom presence detection with a 95% fidelity. We optimize the position of the gold knife edge to homogenize the response of the two traps. The measured mean bright-state counts differ by 5% between the two traps and the atom presence detection fidelity differs by 0.5%. While increasing the detection pulse duration improves fidelity, it also increases heating due to photon scattering which leads to atom loss. Choosing a shorter detection pulse reduces the probability to lose an atom allowing for the reuse of an atom over multiple iterations.

The trap-loading phase of the experiment can limit our bandwidth by consuming around 97% of the duty cycle. To mitigate this reduced bandwidth, we capitalize on atom reuse by employing a field-programmable gate array (FPGA) based control system for high-speed Boolean logic. The FPGA control system allows us to increase our data rate from the 1-Hz level to a maximum of 70 Hz for single-atom experiments. The logic implements a high-speed flow chart that responds appropriately to outcomes of the detection sequence. When the atom is not detected during the check sequence, a more robust check for atom presence is performed immediately. The robust check stage consists of a maximum of three MOT beam pulses identical to the pulse used for detection. If the atoms are observed during the detection pulse or any of the pulses during the check sequence, then the entire experimental cycle is repeated, skipping the rate-limiting trap-loading phase. Otherwise, the MOT is repopulated to reload the traps. Heating induced by the detection beam is minimized by using the minimum number of pulses required to verify atom presence. The actual data rate depends on the specifics of the experiment. We achieve a 70-Hz data rate when performing single-atom, state-selective, lossless detection experiments similar to those described in [29,30]. When implementing experiments with loss-based detection techniques, the data rate is lower and depends on the experiment-specific loss rate. For example, the average data rate for the experiments detailed in Secs. V and VI are 2 Hz (Fig. 4), 0.7 Hz (Fig. 7, single atom), and 0.3 Hz (Fig. 7, two atoms). The data rate in these experiments can, in principle, be greatly improved by combining lossless detection techniques with the transfer of Rydberg state population to $|6S_{1/2}, F = 3, m_F = 0\rangle$ [5].

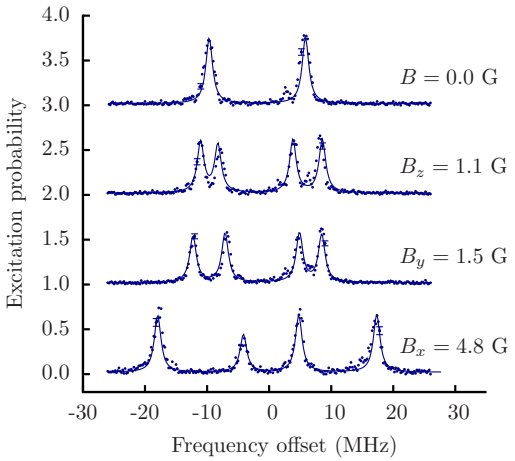

FIG. 4. (Color online) Spectroscopy of the $84P_{3/2}$ state for various bias magnetic fields **B**. From top to bottom, the spectrum is shown for **B** = (0,0,0), (0,0,B_z), (0,B_y,0), and (B_x,0,0) where the x, y, and z axes are labeled in Fig. 3. The solid blue line represents a model for the spectrum that includes perturbations to the state due to the presence of magnetic and electric fields. A fit of the model to the data using the magnitude and direction of $\mathcal{E}$ as free parameters indicates the presence of a 6.35(5)-V/m electric field collinear with the z axis (normal to the dipole trap lens) with a $\pm 20^\circ$ uncertainty. The spectra are offset by multiples of 1.0 on the y axis of the plot for clarity.

V. ELECTRIC FIELD ENVIRONMENT

Rydberg electron wave functions scale to extremely large sizes with increasing n. Consequently, dipole matrix elements between adjacent states grow as well, scaling like $n^2 a_0 e$ [31], where a_0 is the Bohr radius and e is the elementary charge. This in turn implies extreme sensitivity to dc electric fields due to increasingly large electric polarizabilities. We calculate that the $84P_{3/2}$ state polarizability α_r is on the order of 10^{11} times larger than that of the ground state. We use this large polarizability to measure the electric field environment at the dipole traps by studying the spectrum of the Rydberg state.

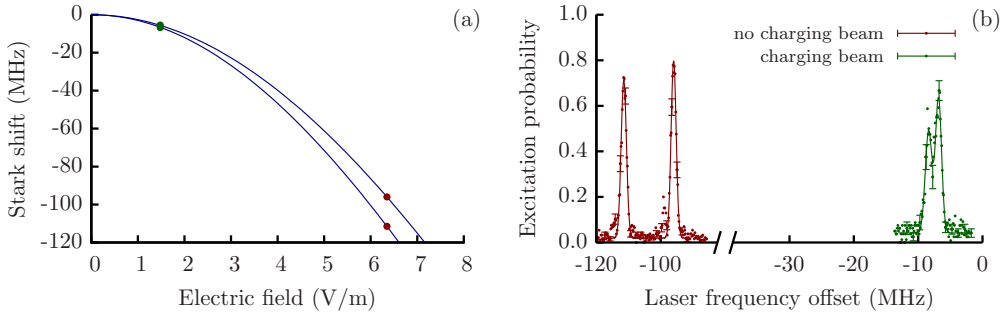

FIG. 5. (Color online) Electric field reduction via controlled surface charging with the charging laser. (a) Calculated Stark shift in the frequency of the $84P_{3/2}$ state with no applied bias magnetic field. (b) Observed spectrum with (green points) and without (red points) the charging laser beam. Measured resonance frequencies are plotted directly on (a) using the same color scheme. The presence of the charging beam reduces the electric field magnitude to 1.5(1) V/m. Error bars shown are representative.

The Rydberg spectrum we measure for $84P_{3/2}$ is shown in Fig. 4. The excitation experiment uses a 580-ns UV laser pulse over a 50-MHz laser frequency scan range. While we expect a single peak in the absence of any external perturbations, the observed spectrum consists of two nondegenerate peaks. The observed degeneracy breaking for the zero magnetic field condition ($B = 0$) in Fig. 4 is the result of a background electric field that shifts the resonances through the dc Stark effect. To further our understanding of the background electric field source, we characterize the Rydberg spectrum at several different bias magnetic field directions and compare the result with a detailed model.

We model the splitting in the four Rydberg resonances by including the perturbing effects of electric and magnetic fields. The relative splitting is calculated by diagonalizing the matrix of the total Hamiltonian

$$H = H_{\text{atom}} + H_{\text{Stark}} + H_{\text{Zeeman}}. \tag{2}$$

Here, H_{atom} is the unperturbed Hamiltonian of a single atom and its matrix elements can be constructed using QDT [15]. The final two terms are given by $H_{\text{Stark}} = -\boldsymbol{\mu}_{\mathbf{d}} \cdot \mathcal{E}$ and $H_{\text{Zeeman}} = -\boldsymbol{\mu}_{\mathbf{m}} \cdot \mathbf{B}$. Here, the electric and magnetic dipole moment operators are given by $\boldsymbol{\mu}_{\mathbf{d}}$ and $\boldsymbol{\mu}_{\mathbf{m}}$, respectively, $\mathcal{E}$ is a dc electric field, and $\mathbf{B}$ is a dc magnetic field. While the strength and direction of $\mathbf{B}$ is controlled using three sets of Helmholtz coils, the electric field is a background intrinsic to our system. We diagonalize Eq. (2) for a set of states large enough to ensure convergence of the eigenvalues and eigenvectors of H over the chosen electric field range. This includes states where n ranges from 81 to 89, and ℓ ranges from 0 to 6. The matrix elements for H_{Stark} and H_{Zeeman} can be calculated with techniques described in [32,33]. A comparison of this theoretical model with experimental data is shown in Fig 4. Using the direction and strength of the electric field as a free parameter, we find that there is a 6.35(5) V/m electric field at the location of the atom, pointed along a direction perpendicular to the lens surface (Fig. 3). This field direction indicates charging of the dipole trap lens.

We observe variation in surface charging with changes in background cesium vapor pressure and dipole trap laser intensity. While the dipole trap laser drives charge production, whose steady-state value increases with laser intensity, the cesium vapor pressure modifies properties of the charging process. We observe that increasing vapor pressure decreases the charging time constant, which ranges from minutes to hours and additionally reduces the field strength. It is known that the density of cesium coverage on a surface modifies the work function [34,35]. Changes to the work function would affect the laser-induced charging and is a likely explanation for the observed trend with cesium vapor pressure. To reduce fluctuations in $\mathcal{E}$, we stabilize the dipole trap laser power and cesium vapor pressure. Even so, this does not eliminate the observed fluctuations in Rydberg state energy. The calculated electric field perturbation approximately follows the quadratic Stark effect as is shown in Fig. 5. Noise in the Stark shift δE_{Stark} increases linearly with electric field noise $\delta\mathcal{E}$, or

$$\delta E_{\text{Stark}} = 2\alpha_r |\mathcal{E}| \delta\mathcal{E}.$$

Therefore, to reduce resonance fluctuations, we introduce a charging laser beam to the experiment to gain leverage over the electric field environment.

The charging beam generates charge on the ITO glass plates at a position chosen to counteract the electric field at the atom as shown in Fig. 3. The exact position and intensity of the charging beam is finely tuned to minimize the electric field at the atom. The result of this process is found in Fig. 5(b), where the spectrum shifts blue and the Stark splitting is reduced. From the measured Stark splitting, we estimate that the electric field at the atom is 1.5(1) V/m. With the introduction of the charging beam, the measured Rydberg resonance has a full width at half maximum of 440(50) kHz. Additionally, measurements of the spectrum over a 9-h time period indicate a characteristic resonance drift of 20 kHz over 30 min. We find that the combination of the ITO coated surfaces enables this stability in our system for high principal quantum number and correspondingly high electric field sensitivity. This is a 100-fold improvement when compared with our previous studies that utilized an identical lens with AR coating on the surface closest to the atom. This improved stability allows for coherent excitation of blockaded Rydberg atoms as is demonstrated in Sec. VI.

VI. RYDBERG BLOCKADE

The Rydberg blockade effect occurs when the EDDI potential energy U_{int} between nearby atoms shifts the doubly excited Rydberg state $|rr\rangle$ out of resonance with the excitation

laser, blocking multiple Rydberg excitations. Producing efficient blockade entails maximizing the interaction potential energy so that $U_{\text{int}} \gg \Omega$. At large interatomic separation R the interaction obeys a van der Waals potential of the form $U_{\text{int}} = C_6/R^6$. From this, we can increase U_{int} by either increasing principal quantum number since $C_6 \propto n^{11}$ [36] or decreasing R. While it is attractive to maximize U_{int} by increasing n, the electric polarizability also rises as n^7 causing the system to be more susceptible to stray electric fields. We consequently target a value of n with manageable dc Stark shift and significant blockade at interatomic distances that are optically resolvable. While we have already shown that the former condition is satisfied for $n = 84$ in Sec. V, the latter can be determined numerically. Therefore, to select a Rydberg state and interatomic separation that satisfies $U_{\text{int}} \gg \Omega$, we numerically calculate the doubly excited Rydberg state spectrum $nP + nP$ as a function of interatomic separation.

The numerical calculation determines the energies and transition oscillator strengths of the sublevels contained within $nP + nP$ as functions of R. The calculation diagonalizes a Hamiltonian that contains electric dipole and quadrupole interactions in a chosen subspace of $nl + n'l'$ state pairs where the primed variables refer to the state of the second atom. As an example, we perform the calculation for the $84P_{3/2}$ states. Because interaction channels $nl + n'l'$ with energies closest to $84P_{3/2} + 84P_{3/2}$ are the largest contributors to the EDDI [8], we perform the calculation for states that span a 40-GHz range centered around this target state and restrict l and l' to 0–5. We find the inclusion of the high angular momentum states necessary as the spectrum becomes heavily mixed and therefore choose the largest range allowed for by our current computational resources. Techniques for computing U_{int} are found in [36–38], and the result closely resembles [38]. We calculate that blockade becomes significant below 7 μm for $\Omega/2\pi = 1$ MHz as is shown in Fig. 6. For the experiment, we choose to use a mean separation of 6.6(3) μm resulting in $U_{\text{int}}/2\pi \sim 6.4$ MHz. The calculation of nonzero blockade for all sublevels appears to be in contradiction with the prediction of Förster zeros (unshifted states) [39] for the $nP_{3/2} + nP_{3/2}$ state studied here. The difference arises because we are concerned with values of R where convergence of the calculation requires multiple $nl + nl \rightarrow n'l' + n''l''$ channels, whereas [39] emphasizes the most significant term at large interatomic separations (van der Waals regime). With an interaction potential on the order of 1 MHz, signatures of Rydberg blockade should be present.

Using our calculation as a guide, we experimentally identify signatures of Rydberg blockade. For the experiment, we resonantly excite $|84P_{3/2}, m_j = 3/2\rangle$ with variable laser pulse duration. We use a 319-nm laser intensity of 9.3 kW/cm^2 to achieve $\Omega = 0.816(4)$ MHz and apply a 4.8-G bias magnetic field to break the degeneracy in m_j. The measured Rydberg excitation probability with single as well as two interacting atoms is shown in Fig. 7(a). The measured ratio of the Rydberg excitation Rabi frequencies $\Omega_{2\text{-atoms}}/\Omega$ is 1.42(2), which is consistent with $\sqrt{2}$. An increase in the excitation Rabi frequency of $\sqrt{2}$ is expected in the strongly blockaded regime where the system oscillates between the ground state and a state that collectively shares a single Rydberg excitation,

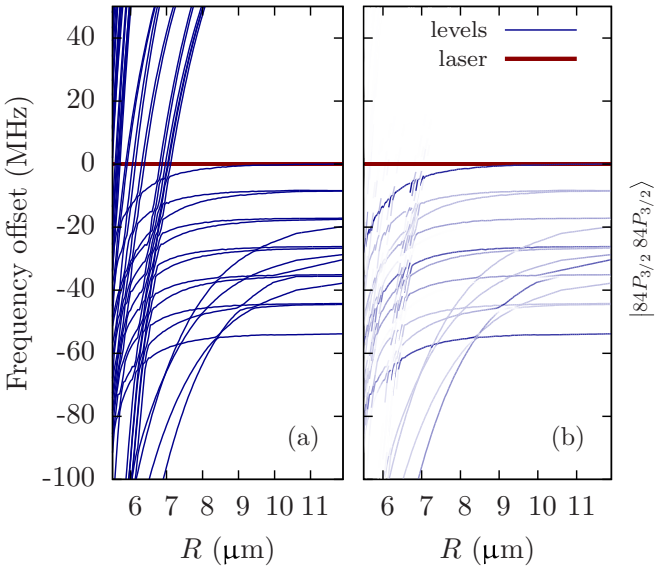

FIG. 6. (Color online) Numerical calculation for the $84P_{3/2} + 84P_{3/2}$ spectrum versus interatomic separation R. The laser is resonant with the unperturbed ($R \rightarrow \infty$) state $|rr\rangle$, where $r \rightarrow \{84P_{3/2}, m_j = 3/2\}$. (a) Frequency offset of all states with respect to r. The excitation range of the Rydberg laser is represented by the position and width ($\sim$ 1 MHz) of the red line. (b) States in (a) with line darkness weighted by the oscillator strength to the ground state ($6S_{1/2}$, $m_F = 0$) for linearly polarized light on the y axis (Fig. 3). We choose to operate at $R = 6.6(3)$ μm to obtain a 6.4-MHz blockade shift. The calculation includes a background electric field $|\mathcal{E}| = 1.6$ V/m and a bias magnetic field $B_x = 4.8$ G as is used in our experiment.

as was first observed by Gaetan *et al.* [4]. Additional evidence of Rydberg blockade is shown in Fig. 7(b) where we plot the two-atom evolution in the basis $\{|gg\rangle, |gr\rangle, |rg\rangle, |rr\rangle\}$. Here, we show that population transfer between the ground state and the singly excited state dominates the system evolution, whereas excitation to $|rr\rangle$ is strongly suppressed. Both plots illustrate coherent control of two strongly blockaded atoms.

The coherent dynamics of this system, with or without two-atom blockade, indicates decoherence dominated by population relaxation Γ_{loss} out of the Rydberg state. We measure $\Gamma_{\text{loss}} = 1.2(1)$ MHz, which is substantially broader than the calculated state linewidth of 4 kHz [40]. The trend in the evolution of the atom towards excitation to $|r\rangle$, shown in Fig. 7, occurs because our detection method can not differentiate between population in $|r\rangle$ and other atom-loss mechanisms. Examples of possible loss sources include an applied force on the center of mass of the atom from an electric field gradient and a reduced state lifetime due to background RF fields. Order-of-magnitude estimates suggest that the latter example is more likely. In future work, we aim to investigate the source of Γ_{loss} and mitigate its decohering effects.

VII. SUMMARY AND OUTLOOK

In summary, we present experiments and theoretical models that focus on Rydberg blockade with a single-photon

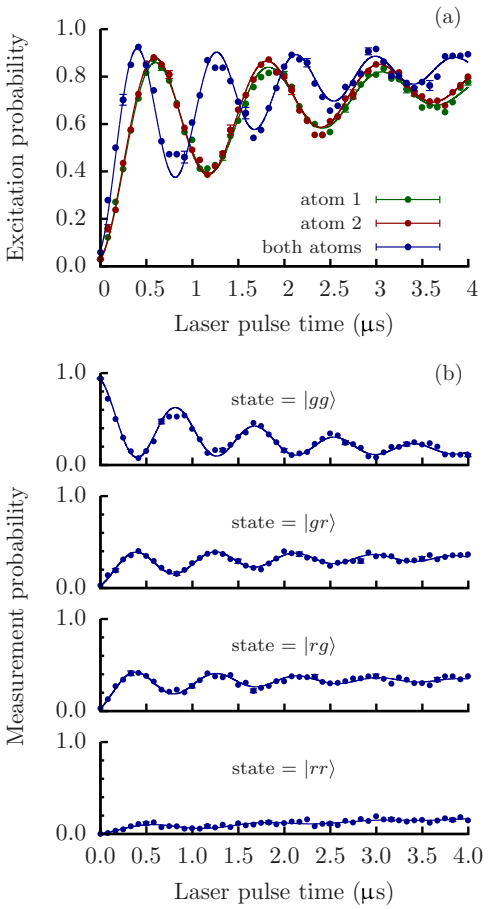

FIG. 7. (Color online) Observation of coherent excitation and Rydberg blockade. (a) Excitation probability for single, noninteracting atoms (atoms 1 and 2) and two interacting atoms (both atoms). The noninteracting data are labeled atom 1 and atom 2, where the number represents exclusive loading of either the first or second dipole trap. Here, the excitation probability P_e is defined as $P_e = 1 - P(|g\rangle)$ for single atoms and $P_e = 1 - P(|gg\rangle)$ for the two-atom case. This plot highlights the $\sqrt{2}$ increase in excitation Rabi frequency of two atoms in the strong blockade regime. (b) Measured evolution of the blockaded two-atom system in the basis $\{|gg\rangle, |gr\rangle, |rg\rangle, |rr\rangle\}$. Error bars shown are representative.

transition. We construct a UV laser for direct excitation to $nP_{3/2}$ Rydberg states and demonstrate the accuracy of our calculations for the Rydberg spectrum and oscillator strength with single-atom spectroscopy. These Rydberg atoms are employed as electric field sensors to study laser-induced charging of nearby surfaces, and we utilize this information to mitigate noise on the Rydberg resonance frequency due to the dc Stark effect. Finally, we model EDDIs for two $84P_{3/2}$ Rydberg atoms as a function of interatomic separation and demonstrate Rydberg blockade through an increase in the collective excitation Rabi frequency.

In principle, this single-photon approach offers an advantage over two-photon Rydberg excitation by eliminating the need for an intermediate state, thus avoiding channels for photon scattering, frequency noise, and dipole forces. Reducing photon scattering is especially attractive for the study of dipolar interactions between Rydberg dressed states, where allowing the system to relax to equilibrium can take on order of 1 ms [10,11]. However, this fundamental limit on the photon scattering rate remains to be demonstrated in our experiment. The moderate increase in Doppler sensitivity when using single-photon Rydberg excitation can be addressed with more advanced cooling techniques, such as ground-state cooling [28,41].

ACKNOWLEDGMENTS

We thank M. Saffman, A. Browaeys, J. Shaffer, S. Rolston, I. Deutsch, T. Keating, and R. Cook for helpful discussions and suggestions. We would also like to thank G. Burns, P. Schwindt, M. Mangan, C. Johnson, and A. Ferdinand for contributions to the experiment. We acknowledge Laboratory Directed Research and Development for funding this work. Sandia National Laboratories is a multiprogram laboratory managed and operated by Sandia Corporation, a wholly owned subsidiary of Lockheed Martin Corporation, for the U.S. Department of Energy's National Nuclear Security Administration under Contract No. DE-AC04-94AL85000.

[1] J. D. Carter and J. D. D. Martin, Phys. Rev. A **88**, 043429 (2013).
[2] A. Tauschinsky, R. M. T. Thijssen, S. Whitlock, H. B. van Linden van den Heuvell, and R. J. C. Spreeuw, Phys. Rev. A **81**, 063411 (2010).
[3] J. D. Carter, O. Cherry, and J. D. D. Martin, Phys. Rev. A **86**, 053401 (2012).
[4] A. Gaetan, Y. Miroshnychenko, T. Wilk, A. Chotia, M. Viteau, D. Comparat, P. Pillet, A. Browaeys, and P. Grangier, Nat. Phys. **5**, 115 (2009).
[5] T. Wilk, A. Gaëtan, C. Evellin, J. Wolters, Y. Miroshnychenko, P. Grangier, and A. Browaeys, Phys. Rev. Lett. **104**, 010502 (2010).
[6] L. Isenhower, E. Urban, X. L. Zhang, A. T. Gill, T. Henage, T. A. Johnson, T. G. Walker, and M. Saffman, Phys. Rev. Lett. **104**, 010503 (2010).
[7] Y. O. Dudin, L. Li, F. Bariani, and A. Kuzmich, Nat. Phys. **8**, 790 (2012).
[8] M. Saffman, T. G. Walker, and K. Mølmer, Rev. Mod. Phys. **82**, 2313 (2010).
[9] T. G. Walker and M. Saffman, in *Advances in Atomic, Molecular, and Optical Physics*, Vol. 61, edited by E. A. Paul Berman and C. Lin (Academic, Oxford, 2012), pp. 81–115.
[10] J. E. Johnson and S. L. Rolston, Phys. Rev. A **82**, 033412 (2010).
[11] T. Keating, K. Goyal, Y.-Y. Jau, G. W. Biedermann, A. J. Landahl, and I. H. Deutsch, Phys. Rev. A **87**, 052314 (2013).
[12] H. Saßmannshausen, F. Merkt, and J. Deiglmayr, Phys. Rev. A **87**, 032519 (2013).
[13] D. Tong, S. M. Farooqi, J. Stanojevic, S. Krishnan, Y. P. Zhang, R. Côté, E. E. Eyler, and P. L. Gould, Phys. Rev. Lett. **93**, 063001 (2004).
[14] M. J. Seaton, Rep. Prog. Phys. **46**, 167 (1983).

[15] K.-H. Weber and C. J. Sansonetti, Phys. Rev. A **35**, 4650 (1987).
[16] M. Fabry, J. Quant. Spectrosc. Radiat. Transfer **16**, 127 (1976).
[17] E. Fermi, Z. Phys. **59**, 680 (1930).
[18] C.-S. O, G. F. Fülöp, O. Redi, and H. H. Stroke, J. Opt. Soc. Am. **71**, 1072 (1981).
[19] J. C. Weisheit, Phys. Rev. A **5**, 1621 (1972).
[20] A. Wilson, C. Ospelkaus, A. VanDevender, J. Mlynek, K. Brown, D. Leibfried, and D. Wineland, Appl. Phys. B **105**, 741 (2011).
[21] The cavity has a finesse of 20 000 at 638 nm. The cavity temperature is stabilized and kept under vacuum at 10^{-7} Torr to reduce environmental effects driving the cavity resonance frequency.
[22] L. P. Parazzoli, A. M. Hankin, and G. W. Biedermann, Phys. Rev. Lett. **109**, 230401 (2012).
[23] The quoted error is derived from focal length and atom motion uncertainty.
[24] L. Béguin, A. Vernier, R. Chicireanu, T. Lahaye, and A. Browaeys, Phys. Rev. Lett. **110**, 263201 (2013).
[25] Fibers are single mode at 1550 nm.
[26] N. Schlosser, G. Reymond, and P. Grangier, Phys. Rev. Lett. **89**, 023005 (2002).
[27] D. J. Wineland, J. Dalibard, and C. Cohen-Tannoudji, J. Opt. Soc. Am. B **9**, 32 (1992).
[28] A. M. Kaufman, B. J. Lester, and C. A. Regal, Phys. Rev. X **2**, 041014 (2012).
[29] A. Fuhrmanek, R. Bourgain, Y. R. P. Sortais, and A. Browaeys, Phys. Rev. Lett. **106**, 133003 (2011).
[30] M. J. Gibbons, C. D. Hamley, C.-Y. Shih, and M. S. Chapman, Phys. Rev. Lett. **106**, 133002 (2011).
[31] T. Gallagher, *Rydberg Atoms*, Cambridge Monographs on Atomic, Molecular and Chemical Physics (Cambridge University Press, Cambridge, UK, 2005).
[32] M. L. Zimmerman, M. G. Littman, M. M. Kash, and D. Kleppner, Phys. Rev. A **20**, 2251 (1979).
[33] I. Hirano, Metrologia **21**, 27 (1985).
[34] J. B. Taylor and I. Langmuir, Phys. Rev. **44**, 423 (1933).
[35] S. H. Chou, J. Voss, I. Bargatin, A. Vojvodic, R. T. Howe, and F. Abild-Pedersen, J. Phys.: Condens. Matter **24**, 445007 (2012).
[36] M. Saffman and T. G. Walker, Phys. Rev. A **72**, 022347 (2005).
[37] T. G. Walker and M. Saffman, Phys. Rev. A **77**, 032723 (2008).
[38] A. Schwettmann, J. Crawford, K. R. Overstreet, and J. P. Shaffer, Phys. Rev. A **74**, 020701 (2006).
[39] T. G. Walker and M. Saffman, J. Phys. B: At., Mol. Opt. Phys. **38**, S309 (2005).
[40] Calculation includes the effect of room-temperature blackbody radiation.
[41] J. D. Thompson, T. G. Tiecke, A. S. Zibrov, V. Vuletić, and M. D. Lukin, Phys. Rev. Lett. **110**, 133001 (2013).